Charging Li Ions with Minimal Energy: A Study on Current Profiles

Qian Zhi and Gabriel A. Rincón-Mora, *Fellow, IEEE*

***Abstract*—Charging batteries in cell phones and other small electronic devices, such as battery banks or laptops, has become increasingly common. Volume and charging efficiency are critical in this space because both source and load lose the energy they need and cannot recover. Charging batteries in a way that maximizes their efficiency is, therefore, as important as transferring energy with efficiency. This research investigates the impact of charge-current profiles on energy savings with over 400 charge-discharge experiments performed on two Li-ion batteries. The investigation is the most comprehensive among the state of the art (SoA) and the only one to effectively normalize the battery's cycle-life effect. Results show that ripple current charging is ineffective in reducing the amount of energy required during the charging process, irrespective of the battery type. Instead, it is recommended to use a dc charge current that is programmed to reduce when extended charge time is available to reduce the energy loss when charging consumer electronics.**

***Index Terms*—Li-ion, optimal charge-current profile, energy efficiency, ac ripple, on-the-go charging, series resistance, cycle life.**

I. Charging Batteries On-the-Go

MANY mobile electronics today, such as cell phones, laptops, tablets, wireless headphones, and gaming consoles, rely on Li-ion batteries for power. Despite continued improvements in energy capacity, batteries remain a limited energy source [1], [2]. When a battery is depleted, it can significantly disrupt a person's daily life, especially in situations where a power outlet is unavailable.

Luckily, charging batteries on the go (OTG) has become widely accessible. For instance, mobile consumer electronics like cell phones, smartwatches, and wireless earbuds can be conveniently charged using the USB ports of larger mobile devices such as laptops, tablets, and battery banks [3]. Fig. 1 illustrates an on-the-go charging system where a charger draws power from the source to replenish the battery of the mobile device and sustain its various functionalities, including amplifiers, digital signal processors (DSPs), power amplifiers, antennas, and data converters.

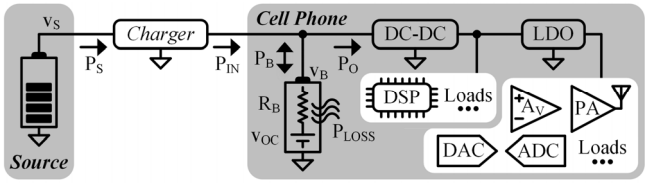

Fig. 1. On-the-go battery-charging system.

The advantage of OTG charging is that it allows a mobile device to continue functioning without an outlet. Since most people carry battery-powered devices today, energy sources are readily available. However, OTG charging imposes more stringent requirements on charging efficiency compared to conventional charging as it relies on a limited energy source.

TABLE I
VARIABLES

Var.	Description	Unit
v_B	Battery terminal voltage	V
v_{OC}	Open-circuit battery voltage	V
i_B	Battery current	A
i_C	Charge current	A
$i_{C(DC)}$	Average charge current	A
$i_{C(AC)}$	Charge current ripple amplitude	A
i_D	Discharge current	A
f_{AC}	Charge current ripple frequency	kHz
t_C	Total charge time	Minutes
t_D	Total discharge time	Minutes
t_{PRE}	Precondition charge region (low SoC)	Minutes
t_{TST}	Main charge region	Minutes
R_B	Battery internal resistance	W
$R_{B(AC)}$	Battery ac resistance	W
q_B	Battery capacity	Ahr
q_C	Supplied charge during charge	Ahr
q_D	Extracted charge during discharge	Ahr
E_C	Energy consumed by battery during charge	J
E_D	Energy supplied by battery during discharge	J
E_{LOSS}	Battery's energy loss in a cycle	J
T_B	Battery temperature	°C
T_{BR}	Battery temperature rise during charge	°C
ΔT_B	Normalized battery temperature rise	°C
η_E	Energy efficiency	%
$\%\eta_E$	Improved energy efficiency	%
η_C	Charge efficiency	%
SoC	State of Charge	%

While traditional approaches to improve charging efficiency focus on increasing the efficiency of the charger, recent studies have revealed the potential to enhance charging efficiency by minimizing the losses within the battery itself. [4], [5] shaped the charge current to carry an ac ripple to reduce the battery's internal resistance and observed reduced charge time and heating. However, these results are challenged by [6]–[8], where ripple charge current resulted in no significant difference or even inferior performance in charge time, battery heating, and energy consumption.

In addition to the conflicting results regarding the effectiveness of ripple charge current, the current state of the art (SoA) studies on optimized charge current profiles are incomplete. Each study focuses on some, but not all, aspects of the charge current profiles. [5] and [7] explored the effects of current ripple frequency and amplitude, but only sinusoidal ripples are tested. [4], [6], and [8] examined multiple ripple waveforms but did not vary the ripple amplitude. Since each

TABLE II
COMMON COMMERCIAL LI-ION BATTERY CHEMISTRIES AND SPECIFICATIONS

	LCO*	**LMO***	**NMC***	**LFP***	**NCA** [19]
Chemistry	$LiCoO_2$	$LiMn_2O_4$	$LiNi_xMn_yCo_zO_2$	$LiFePO_4$	$LiNi_aCo_bAl_cO_2$
Nominal Capacity	2500 mAh	2500 mAh	3500 mAh	1800 mAh	3350 mAh
Operating Voltage	2.5–4.2 V	2.75–4.2 V	2.5–4.2 V	2.5–3.65 V	2.5–4.2 V
Std. Charge Current	1.75 A (0.7C)	1.25 A (0.5C)	1.7 A (0.5C)	N/A	1.625 A (0.5C)
Max. Charge Current	N/A	4 A (1.6C)	3.4 A (1C)	1.8 A (1C)	N/A
Internal Resistance	N/A	20 mΩ**	40 mΩ (ac)	40 mΩ**	140 mΩ (ac)***
Charge Temp.	10–45°C	0–50°C	0–45°C	0–50°C	0–45°C
Cycle Life	300	N/A	400	2000	500
Part Number	UR18650NSX	IMR18650-2500-35	INR18650 MJ1	HDCF18650-1800	NCR18650B

*Chemistries for commercial batteries specified by retailers. **Measurement methods not specified. ***Measured in the lab

study employed a unique setup, it is challenging to generalize conclusions across these studies. Furthermore, none of the studies normalized the battery's cycle-life effect, which can influence the accuracy of the results as the battery is cycled.

This work aims to enhance the charging efficiency to meet the requirements for consumer electronics OTG charging by optimizing the charge current profiles for Li-ion batteries. The contributions of this research are threefold: (1) presenting the most comprehensive investigation on Li-ion charge-current profiles with over 400 charge-discharge cycles performed on two types of Li ions, (2) improving result accuracy by effectively normalizing the battery's cycle-life effect, and (3) contributing large amount of data points to support the conclusion on ripple-current charging's effectiveness.

The remainder of the paper is organized as follows: Section II discusses the general procedures, requirements, and considerations for charging Li ions. Section III presents the test plan designed to investigate the optimal charge-current profiles. The experimental setup is described in Section IV. Section V presents the results of the battery experiments and compares them with the SoA. Section VI concludes the paper.

II. CHARGING LI IONS

A. Requirements

Voltage: Li-ion batteries operate within a strict voltage range specified by the manufacturers depending on the cathode chemistries [11]–[13]. Table II compares five commercial cylindrical 18650 Li-ion cells. The most common voltage range is 2.5 to 4.2 V for LCO, LMO, NMC, and NCA batteries. LFP cells, on the other hand, operate within a lower voltage range of 2.5 to 3.65 V.

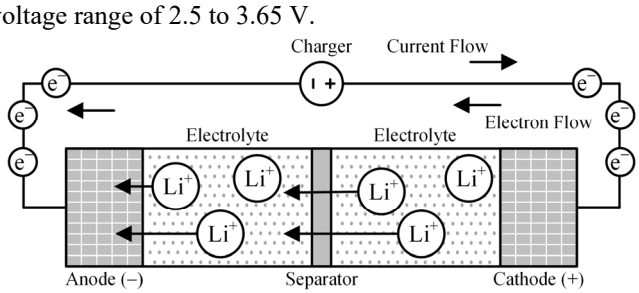

Fig. 2. Li-ion battery operation during the charging process.

Li-ion batteries operate by transporting and storing lithium ions in the electrodes [14], [15]. Fig. 2 illustrates a Li-ion battery's operation during the charging process. When a charge current is applied, Li ions stored in the cathode move towards the anode through the electrolyte and separator. The Li ions then absorb the electrons from the charge current and intercalate into the anode. This processed is reversed during discharge. The Li ions stored in the anode travel to the cathode and create free electrons, which generates a current to supports external loads.

When a battery is overcharged, more Li ions are delivered to the anode than it can accept. This can result in adverse effects including thickened solid electrolyte interphase (SEI) layer [16], increased internal resistance, capacity loss due to lithium plating, and even internal short circuits [17], [18]. Similarly, when a battery is overdischarged, the amount of Li ions delivered to the cathode surpasses its capacity. The resulting adverse effects include SEI layer decomposition, copper current collector oxidation at the anode, capacity loss due to lithium plating, and internal short circuits [17], [20], [21].

Current: Charge current i_C is often specified in C-rate, where 1C corresponds to the current that fully charges a battery within one hour. Table II shows that the recommended i_C is around 0.5C for commercial batteries. There are two primary concerns associated with higher i_C. Firstly, a higher charge current can lead to the accumulation of Li ions at the rate-limiting step of the charging reaction. This can result in undesirable effects like lithium plating and the subsequent capacity loss. Secondly, a high i_C value can generate excess heat due to the battery's internal resistance (R_B). This places additional stress on the device's heat management system.

Temperature: All the batteries in Table II require charging at temperatures above 0 °C. Low temperature hinders the charging process for several reasons. Firstly, at lower temperatures, the viscosity of the electrolyte increases, along with the internal resistance of the battery. This impedes the charge-transfer reactions and reduces the diffusion rate of Li ions within the electrodes. The slow intercalation of Li ions into the electrodes increases the risk of lithium plating and irreversible capacity loss [22]–[24].

The maximum temperature for the batteries in Table II is typically limited to around 45 °C. This is because high temperatures accelerate the aging process of a battery, leading to a decrease in its overall lifespan [25]. Additionally, elevated temperatures can trigger exothermic reactions within the battery, potentially resulting in thermal runaway [26], [27]. This positive feedback loop increases the pressure inside the

battery and can result in flames and explosions [14], [22].

B. Considerations

Internal Resistance: The internal resistance (R_B) encompasses all the resistances on conduction path of a battery current. R_B adds an ohmic voltage component (v_R) to the battery's terminal voltage (v_B) during the charging process:

$$v_B = v_{OC} + v_R = v_{OC} + i_C R_B \,. \tag{1}$$

This is in addition to the battery's open-circuit voltage (v_{OC}) at equilibrium. A high R_B prolongs the charge time because v_B will reach the maximum voltage faster, at which point the charge current must be decreased to prevent the battery from being damaged. The loss across R_B also reduces the power delivered to the battery, thereby decreasing the charge speed. Effective management of R_B's heat dissipation is also crucial to prevent the battery from overheating.

State of Charge (SoC): The SoC of a battery indicates the fraction of available charge compared to its full capacity:

$$\mathrm{SoC} = \mathrm{SoC}_0 + \frac{\Delta q_X}{q_B} = \mathrm{SoC}_0 + \frac{\int_0^{t_X} i_B dt}{q_B}, \tag{2}$$

where SoC_0 is the battery's initial SoC, and Δq_X is the amount of charge injected or extracted by current i_B during t_X. q_B is the battery's capacity found by integrating the discharge current i_D over the discharge time t_D during a complete discharge:

$$q_B = \int_0^{t_D} i_D dt \,. \tag{3}$$

If SoC_0 and i_B are known, a battery's SoC at any instance can be calculated through the current integration technique [28].

SoC reflects a battery's energy level and allows users to estimate the remaining charge time. Certain battery parameters, such as R_B, are also sensitive to the SoC. At extremely low SoCs, R_B is often significantly higher, which requires trickle charging to prevent damaging the battery. Operating a battery at extreme SoCs can also accelerate its aging, which is typically avoided.

Cycle Life: The cycle life of a battery refers to the number of charge-discharge cycles it can undergo before experiencing a significant reduction in its capacity. As the battery ages, its performance gradually deteriorates [29], [30]. Fig. 3 illustrates an NCR18650B battery's cycle life. Across 500 cycles, the battery capacity (q_B) decreases by approximately 30%. As a battery ages, R_B also increases, which causes larger heat dissipation that further accelerates aging.

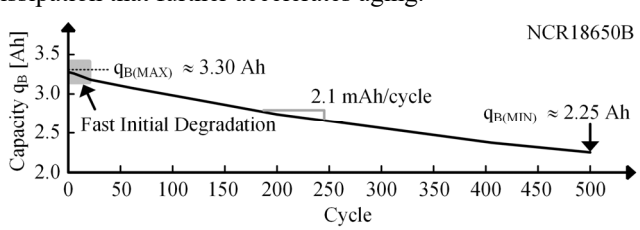

Fig. 3. Specified capacity across cycle life.

C. Typical Charge Profiles

Constant Current-Constant Voltage (CC–CV) is the most common charging profile. Fig. 4 depicts a typical cycle using a CC–CV charge and CC discharge. The cycle is comprised of five regions: CC charge ($t_{C(CC)}$), CV charge ($t_{C(CV)}$), rest (t_{R1}), discharge (t_D), and rest (t_{R2}). During $t_{C(CC)}$, a constant current ($i_{C(CC)}$) is applied to charge the battery until v_B reaches the upper limit (v_{CV}). During $t_{C(CV)}$, v_B is held constant while the charge current is reduced to the cutoff level (i_{CO}). During the discharge phase, a constant current i_D discharges the battery, reducing v_B to the cutoff voltage (v_{CO}).

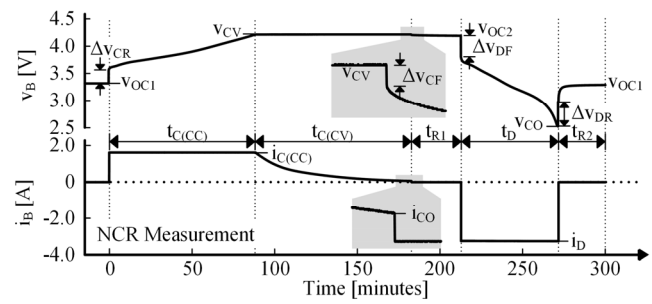

Fig. 4. Typical cycle with CC–CV charge and CC discharge.

The rest periods (t_{R1} and t_{R2}) allow the battery to undergo relaxation and reach internal equilibrium. During this time, v_B approaches the open circuit voltage [31]. The sharp voltage rises/falls (Δv_{CR}, Δv_{CF}, Δv_{DF}, and Δv_{DR}) observed during these periods are caused by the ohmic component of R_B.

The CC–CV charging profile offers two advantages. Firstly, it is relatively simple to implement as it only requires regulating either i_B or v_B to a constant value. This simplicity reduces the design complexity and the cost of the charger. Secondly, the CV phase ensures full charging of the battery without exceeding the specified voltage limits by reducing i_B and the associated voltage drop across R_B.

III. Test Plan

A. Battery Selection

Due to time constraints, two batteries (NCR18650B and IMR18650) are selected from Table II for detailed investigation. NCR is chosen for its relatively higher R_B, which suggests the potential for more energy improvement with optimized charge profiles. IMR is selected for its high maximum i_C, enabling faster charging and shortened test time.

B. Charge-Current Profiles

The tested charge-current profiles comprise both a dc and an ac component, as depicted in Fig. 5. Four variables that determine the shape of the charge current are investigated: ripple waveform, ripple frequency, ripple amplitude, and average current level. The ripple current profiles are applied individually to two regions distinguished by the battery's behaviors during the charge cycle.

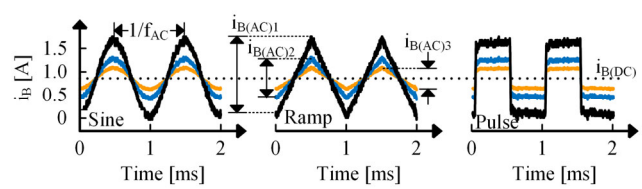

Fig. 5. Charge-current profiles with ac ripples.

Waveform: Three ac waveforms proposed in the SoA are explored: sine, ramp, and pulse. A sine ripple, having only one

frequency component, can establish a direct connection between ripple frequency and any potential improvement. Ramp ripples are studied due to their resemblance to the shape of the inductor current in DC–DC converters. Pulse ripples, on the other hand, are tested because they allow for periods of rest during which charges can settle within the battery [32].

Frequency: The ripple's frequency f_{AC} in Fig. 5 is investigated because the internal resistance has an ac component ($R_{B(AC)}$) that is sensitive to frequency. In Fig. 6, $R_{B(AC)}$ for NCR is measured from 5 Hz to 100 kHz with 10 data points per decade at five different SoCs. The results consistently show a minimum $R_{B(MIN)}$ of about 137 mΩ at a frequency $f_{R(MIN)}$ of around 4-5 kHz. For IMR, the measured value of $R_{B(MIN)}$ and $f_{R(MIN)}$ are 35.2 mΩ and 2.6 kHz, respectively.

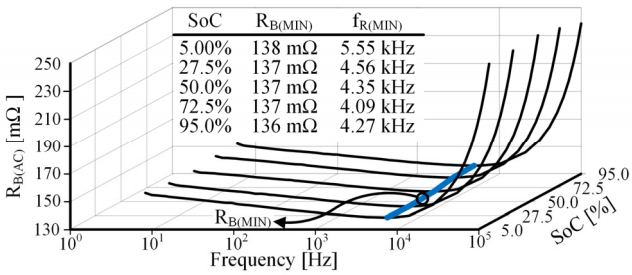

Fig. 6. Measured ac resistance for NCR18650B.

The frequencies tested are chosen to be close to $f_{R(MIN)}$ for the highest chance of energy savings from minimizing $R_{B(AC)}$. Initially, a larger number of frequencies are investigated. As the result trends become established, the number of tested frequencies is reduced to save test time. For NCR, the initial tests explore 10 frequencies ranging from 1 kHz to 10 kHz. Based on the observed trends, the number of frequencies is later reduced to three: 2 kHz, 4 kHz, and 6 kHz. Similarly, ripples are mostly tested at 1 kHz, 3 kHz, and 5 kHz for IMR.

Amplitude: In the existing literature, the effect of ripple peak amplitude $i_{C(AC)}$ is rarely explored. This study investigates $i_{C(AC)}$ at 10%, 25%, 50%, and 100% of the average charge current $i_{C(DC)}$. These values are chosen arbitrarily to cover a range of amplitudes and explore their impact on charging efficiency. As the study progresses and the result trends become apparent, the number of $i_{C(AC)}$ values tested is reduced to save time.

DC Level: DC charge current $i_{C(DC)}$ is rarely investigated in the SoA. In this experiment, the maximum $i_{C(DC)}$ is chosen to ensure that the instantaneous charge current does not exceed the limits specified by the datasheet of the batteries. For NCR, $i_{C(DC)}$ is tested at 406 mA, 609 mA, and 813 mA. For IMR, $i_{C(DC)}$ is investigated at 500 mA and 1000 mA.

Precondition: v_B typically rises faster when the charge current is first applied. This is because the charge-transfer and diffusion reactions in the battery are still approaching the steady-state [33], so the internal resistance is higher. For a more controlled experiment, this initial period (t_{PRE}) with fast v_B is investigated separately from the rest of the charge cycle (t_{TST}). t_{PRE} and t_{TST} are separated by visually observing v_B's rate of change during the charging process. t_{PRE} is determined to be 10 minutes for NCR and 8.3 minutes for IMR.

C. Test Flow

The batteries are investigated according to the test flow in Fig. 7. Initially, a preconditioning phase is conducted to cycle the new battery through its initial cycles, which helps mitigate any variations in battery properties caused by factors like the formation of the solid electrolyte interface (SEI) layer [16]. If the capacity decay of the test battery does not stabilize within 10 cycles, it is considered faulty and replaced.

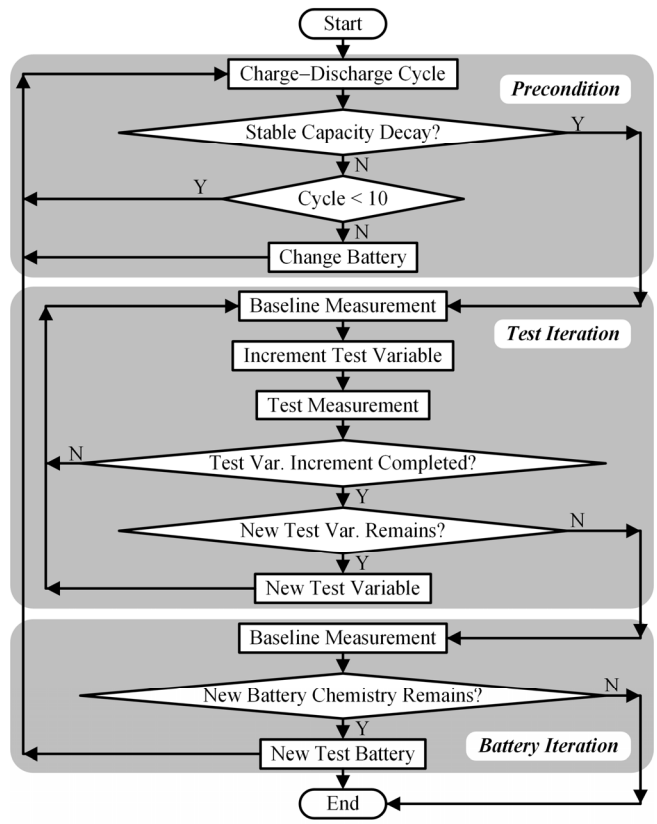

Fig.7. Test Flow.

The preconditioned battery then enters the main test iteration, where alternating baseline and test measurements are performed. During the baseline measurements, the battery is charged with the conventional dc current. In contrast, during the test measurements, the battery is charged using the ripple charge current profiles shown in Fig. 5. By comparing the test measurement results with the baseline measurement results, any potential improvement resulting from the investigated charge-current profile can be revealed.

To isolate the effects of the variables, only one variable is incremented at a time. For example, the ripple frequency is increased at each test measurement while the ripple amplitude, waveform, average current level, and applied region remain constant. After all the ripple frequencies are explored, another variable is incremented in a similar manner. This process continues until each charge-current variable has been investigated for every battery.

D. Charge-Discharge Cycle

The experiments conducted in this study utilize a modified charge-discharge cycle shown in Fig. 8 instead of the conventional cycle in Fig. 4. The modified cycle is divided into five distinct regions: charge (t_C), rest (t_{R1}), CC discharge ($t_{D(CC)}$), CV discharge ($t_{D(CV)}$), and another rest period (t_{R2}).

There are two notable differences between the cycle shown in Fig. 8 and the one depicted in Fig. 4. Firstly, a CC charge of fixed duration is employed in Fig. 8 instead of a full CC–CV charge to save time. This partial CC charge is utilized to charge the battery to a fixed predetermined level. Secondly, a CC–CV discharge is employed in place of the CC discharge to reduce the voltage drop (Δv_{DR}) and alleviate the subsequent relaxation process. This modification ensures better control over the initial condition (v_{OC1}) of the battery across cycles.

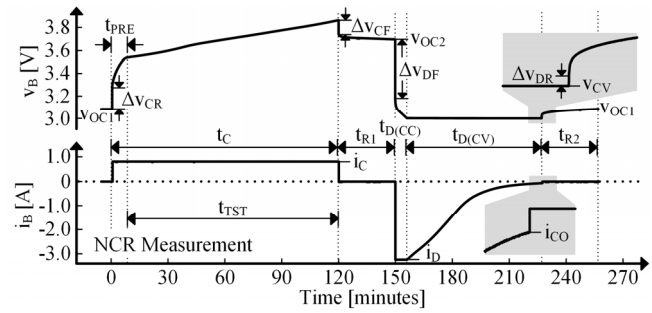

Fig. 8. Test cycle with CC charge and CC–CV discharge.

E. Metrics

Energy efficiency is the primary metric used to investigate the effectiveness of a charge-current profile:

$$\eta_E \equiv \frac{E_D}{E_C} = \frac{\int_0^{t_D} P_D dt}{\int_0^{t_C} P_C dt} = \frac{\int_0^{t_D} i_D v_B dt}{\int_0^{t_C} i_C v_B dt}, \tag{4}$$

where E_C is the charge energy, E_D is the discharge energy, P_C is the charge power, P_D is the discharge power, t_C is the charge time, and t_D is the discharge time. η_E represents how efficiently the battery receives, holds, and delivers energy.

Fig. 9 illustrates the process of tracking and normalizing the battery's cycle-life effect through alternating baseline and test measurements. In the baseline measurements, the battery is charged using constant current. In the test measurements, ac ripples are applied to the charge current. The battery is always discharged using the same CC-CV profile to ensure fair comparisons across measurements.

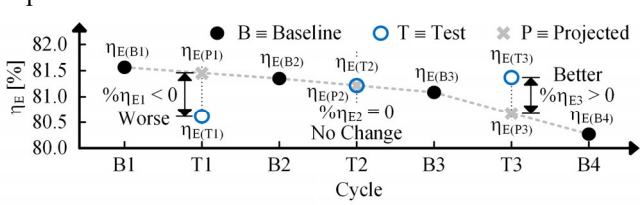

Fig. 9. Cycle-life normalization.

The projected energy efficiency $\eta_{E(P)}$ is used to anticipate the energy efficiency for a test measurement when a dc charge current is used. $\eta_{E(P)}$ can be calculated by averaging the energy efficiency $\eta_{E[B(N)]}$ and $\eta_{E[B(N+1)]}$ from the adjacent baseline trials:

$$\eta_{E(P)} \equiv \frac{\eta_{E[B(N)]} + \eta_{E[B(N+1)]}}{2}. \tag{5}$$

$\eta_{E(P)}$ accounts for the performance degradation caused by the cycle-life effect. By investigating the difference ($\Delta\eta_E$) between the measured energy efficiency $\eta_{E(T)}$ and the projected energy efficiency $\eta_{E(P)}$ for a test measurement, the cycle-life effect is normalized. $\Delta\eta_E$ is expressed as a percentage of the projected energy efficiency to reveal the percentage improvement $\%\eta_E$:

$$\%\eta_E \equiv \frac{\Delta\eta_E}{\eta_{E(P)}} \equiv \frac{\eta_{E(T)} - \eta_{E(P)}}{\eta_{E(P)}}, \tag{6}$$

$\%\eta_E$ represents the extend to which the applied charge current profile improves the energy efficiency of a charge-discharge cycle. For example, a $\%\eta_E$ of 5% indicates that the applied charge current profile improves the energy efficiency by 5% compared to a conventional CC charge.

IV. Tester

A. Requirements

The tester in [10] is fabricated to perform battery experiments. Table III outlines the requirements of this tester. To accommodate the batteries specified in Table II, the tester must support battery voltage ranging from 2.5 to 4.2 V and battery current from –3.3 to 3.3 A. The tester also needs to provide precise output current regulation up to 6 kHz to investigate high-frequency charge-current components

To obtain accurate experiment results, the output current error i_E must be kept below 0.5%. This error is controlled by the current regulation loop gain, denoted as A_{LG} [34]:

$$i_E = i_R - i_{FB} = \frac{i_R}{1 + A_{LG}}, \tag{7}$$

where i_R is the reference current and i_{FB} is the feedback current. To suppress the current error to $i_R/1000$, the low-frequency loop gain (A_{LG0}) needs to be approximately 60 dB. Assuming a dominant pole p_1 at 6 kHz, the current loop's 0-dB bandwidth f_{0dB} is projected to be 6 MHz:

$$f_{0dB} \approx GBW = A_{LG0} p_1, \tag{8}$$

where GBW is the gain bandwidth [34].

The tester's slew rate (SR) must also be high enough to preserve the shape of high-frequency current waveforms. Specifically, for pulse waveforms with sharp transitions, the rise time of the battery current should be a small fraction of the period. For the worst-case scenario of a 6 kHz pulse ripple with an amplitude of 1 A, the required slew rate is 120 mA/µs.

TABLE III
Measured Tester Performance

	Variable	Requirements	Performance
Battery Voltage	v_B	2.5 to 4.2 V	2.5 to 4.2 V*
Battery Current	i_B	–3.3 to 2.0 A	–3.3 to 2.0 A*
Ripple Freq.	f_{AC}	6 kHz	10 kHz
0-dB BW	f_{0dB}	6 MHz	10 MHz
Slew Rate	SR	120 mA/µs	140 mA/µs
Voltage Error	ε_V	0.25%	0.05%
Current Error	ε_I	0.50%	0.46%

*Tested values instead of absolute limits.

B. Prototype

The tester setup consists of a PCB that incorporates a linear charger and discharger, as illustrated in Fig. 10. The overall setup is completed by various benchtop instruments, as shown in Fig. 11. Power supplies are used to provide v_{DD} and v_{SS} for the charger and discharger. Function generators are used to generate reference voltages v_{RH}, v_{RL}, v_{BH}, and v_{BL}.

Specifically, v_{RH} and v_{RL} control the charge and discharge currents, while v_{BH} and v_{BL} limit the battery voltage during the charge and discharge process.

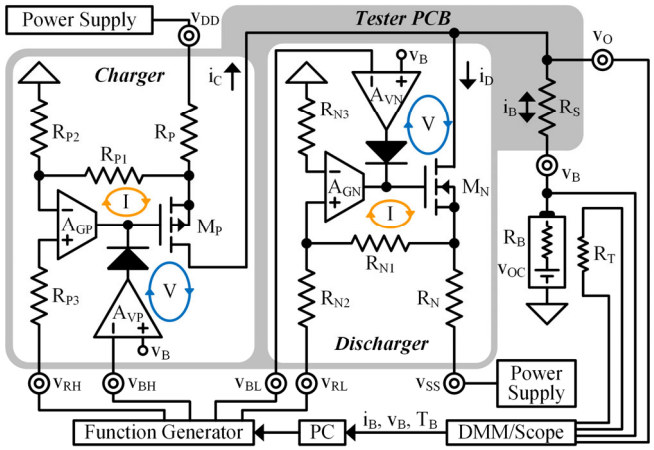

Fig. 10. Battery tester schematic.

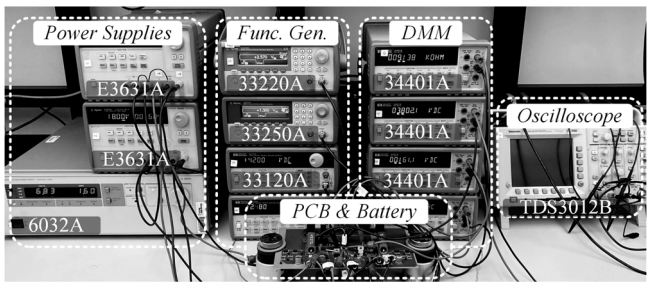

Fig. 11. Experiment setup photo.

The battery current (i_B) and temperature (T_B) are converted to voltages using current-sense resistor R_S and thermistor R_T. These voltage signals are then sensed along with v_B by digital multimeters (DMMs) and oscilloscopes. The DMMs collect the average values of i_B and v_B, while the oscilloscopes periodically capture high-frequency profiles (every 30 seconds) for further analysis.

Both the charger and discharger incorporate a current loop and a voltage loop, as depicted in Fig. 10. The current loop is responsible for regulating i_B when v_B is not close to the upper or lower threshold. On the other hand, when the battery is almost fully charged or discharged, the voltage loops take over to regulate v_B and supply the necessary current for CV charging or discharging. The transition between current and voltage regulation is automatically handled by the feedback loops within the system. A more comprehensive analysis of the system's operation is presented in [10].

C. Performance and Limitations

The measured tester performance is presented in Table III. The tester can support v_B ranging from 2.5 to 4.2 V and i_B from −3.3 to 3.3 A. While the tester can accommodate a wider voltage and current range, these limits were not tested due to the specified limits of the batteries used in this study. The absolute voltage limits are restricted by the v_{DD} and v_{SS} supplies, while the absolute current limits are constrained by the heating of components such as M_P, M_N, R_P, and R_N.

The tester is able to generate ac current waveforms without significant distortion up to a frequency of 10 kHz. LTspice simulation results indicate that the current loop's 0-dB bandwidth is 10 MHz. The slew rate of the tester, measured through step responses, is found to be 140 mA/µs. The maximum applied voltage and current errors are measured to be 0.05% for a standard current of 1.63 mA and 0.46% for a CV charge at 4.2 V. These results demonstrate that the tester meets the requirements for conducting accurate experiments.

The tester has two main limitations. Firstly, the current levels supported by the tester are restricted because linear regulators have relatively low efficiencies. Secondly, the temperature measurements cannot accurately reflect the battery's internal temperature because the thermistor is placed on the surface of the battery cell.

V. Battery Experiment Results

A. DC Level

The effect of average charge current levels $i_{C(DC)}$ on charging efficiency is investigated through the results of the baseline measurements. In these measurements, only a dc charge current is applied to the battery. It is important to note that the battery is supplied with the same amount of charge within each charge cycle for fair comparisons. The measured charge energy (E_C), discharge energy (E_D), and energy efficiency (η_E) for NCR are presented in Fig. 12(a). Each data point represents the average value obtained from 10 cycles.

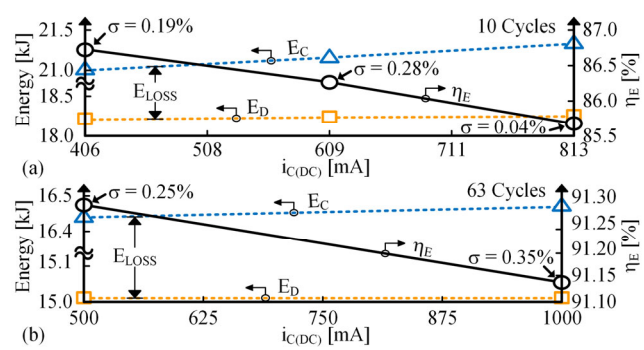

Fig. 12. Effect of dc charge current for (a) NCR and (b) IMR.

The results reveal that as the average charge current increases, the energy required to supply the battery with the same amount of charge also increases. In contrast, the energy extracted during discharge is independent of the average charge current. Consequently, the energy lost in the overall charge-discharge cycle, represented by the parameter E_{LOSS}, increases with higher average charge currents.

A higher average charge current is less efficient because most of the energy loss is caused by the battery's internal resistance R_B. R_B's ohmic loss P_{RB} increases quadratically with the average charge current:

$$P_{RB} = i_{C(DC)}^{2} R_B \propto i_{C(DC)}^{2}, \tag{9}$$

while the charge time decreases linearly:

$$t_C = \frac{\Delta q_B}{i_{C(DC)}} \propto i_{C(DC)}^{-1}. \tag{10}$$

As a result, the total energy E_{RB} lost through the internal resistance, which combines both the ohmic loss and the charge time, scales proportionally with the average charge current:

$$E_{RB} = P_{RB} t_C \propto i_{C(DC)} . \quad (11)$$

Similar trends can be observed for IMR across 63 cycles, as shown in Fig. 12(b). As the average charge current increases from 500 mA to 1000 mA, the required charge energy slightly increases from 16.44 kJ to 16.47 kJ. Consequently, energy efficiency decreases from 91.30% to 91.14%. The energy efficiency has smaller variations due to IMR's lower R_B.

B. AC Ripples

The energy efficiency results from the test measurements, where ripple charge current is applied, are normalized against the baseline measurements using the procedures described in Section III.E. The resulting improved energy efficiency $\%\eta_E$ are shown in Fig. 13–15. Given the significance of the charge current ripple's amplitude and frequency in this study, the improved energy efficiency is plotted against both variables and creates "slices" of data.

In Fig. 13(a), the impact of charge current ripples on the energy efficiency improvement for NCR is illustrated. The ripple amplitude $i_{C(AC)}$ is represented as a percentage of the average charge current $i_{C(DC)}$, ranging from 25% to 100%. The ripple frequency is varied from 2 kHz to 4 kHz. Across all three tested ripple waveforms, $\%\eta_E$ values are mostly close to zero or negative. This indicates that the application of ripple charge current is ineffective in reducing energy loss during the charging process. Furthermore, since most of the energy loss in the battery is attributed to its internal resistance, it can be inferred that the battery's internal resistance does not significantly decrease in response to a charge current ripple.

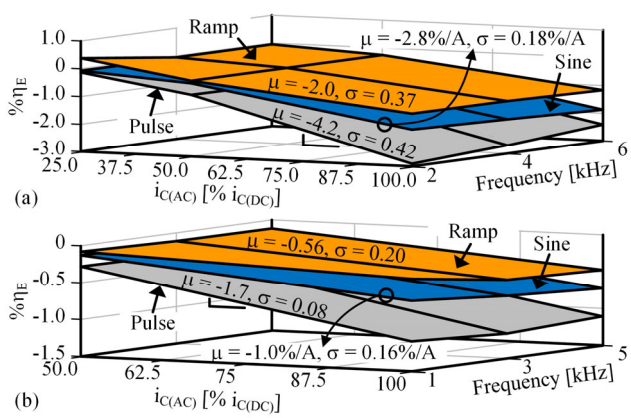

Fig. 13. Effects of ac ripples for (a) NCR and (b) IMR.

$\%\eta_E$ consistently decreases with higher ripple amplitudes. The mean (μ) and standard deviation (σ) of $\%\eta_E$'s rate of change with respect to $i_{C(AC)}$ are marked in Fig. 13(a). $\%\eta_E$ is the most sensitive to ripple amplitude when pulse ripples are applied. Increasing the ripple amplitude from 50% to 100% results in an energy efficiency degradation of around 2%. On the other hand, $\%\eta_E$ is less sensitive to ramp ripple amplitude. This is because pulse ripples carry more energy, as shown by their higher RMS values, compared to a ramp ripple with the same peak amplitude. Since ripple charge current does not reduce the internal resistance, higher RMS ripples will result in higher ohmic loss.

Across ripple frequency, $\%\eta_E$ shows negligible change. This is because the RMS value of a continuous ac ripple is solely dependent on the peak amplitude. Consequently, the energy lost by ripples with the same amplitude but different frequencies remains unchanged. Similar results were observed in the experiment with IMR, as depicted in Fig. 13(b).

The reason that ripple current does not improve the charging efficiency is because only the battery's ac resistance is shown to be sensitive to frequency in Fig. 6. However, only the ac component of the current passes through the ac resistance, and it does not contribute to charging since the average value is zero. The ac current primarily charges and discharges the double layer capacitance at the electrode and electrolyte interface, and the Li ions do not intercalate into the electrodes [6].

In contrast, the average charge current that flows through the battery's dc resistance charges the battery. The dc current prompts the Li ions to participate in a series of electrode reactions and fully intercalate into the anode material, as illustrated in Fig. 2. Because the ac and dc current paths in the battery are different, their corresponding resistances are unlikely to correlate. Because the dc resistance is unaffected by the charge current ripples, applying a charge current ripple is ineffective in improving charging efficiency.

Ripple charge current is also applied to the battery during t_{PRE} when the battery is almost empty because the internal resistance behaves differently at low SoC levels. The results are shown in Fig. 14. $\%\eta_E$ is within ±0.25% for both batteries. This suggests that applying ac ripples does not lead to a significant and long-lasting reduction in the internal resistance and is ineffective in improving charging efficiency when applied at low SoC levels.

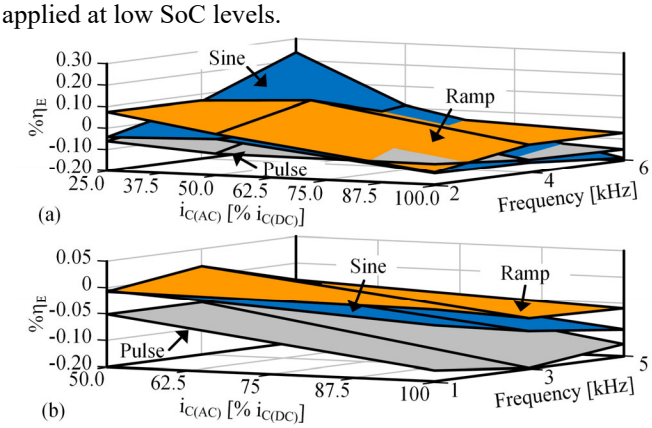

Fig. 14. Effects of ac ripples at low SoCs (a) NCR and (b) IMR.

The effectiveness of ripple charge current is further investigated at different average current levels, and the results are shown in Fig. 15. Similar to the results in Fig. 13, the improved energy efficiency decreases with larger ripples and remains constant across frequencies. Additionally, higher average current levels resulted in lower $\%\eta_E$. This is because the ripple amplitudes are controlled as a percentage of the average charge current, so trials with higher average charge current have larger absolute ripple amplitudes. Therefore, the additional energy consumed by larger ac current ripples reduces $\%\eta_E$.

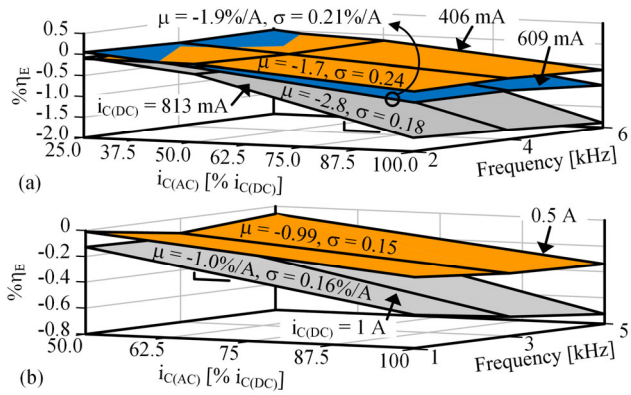

Fig. 15. Effects of ac ripples at various dc levels. (a) NCR. (b) IMR.

To assess the dissipation of energy lost as heat, the temperature rise of the battery during the charging process (T_{BR}) is analyzed. To account for the cycle-life effect, the projected temperature rise ($T_{BR(P)}$) for a test measurement can be calculated by averaging the temperature rises observed in the adjacent baseline measurements ($T_{BR[B(N)]}$ and $T_{BR[P(N+1)]}$):

$$T_{BR(P)} \equiv \frac{T_{BR[B(N)]} + T_{BR[B(N+1)]}}{2}. \tag{13}$$

The battery's temperature rise during a test measurement ($T_{BR(T)}$) is then compared with the projected temperature rise. The resulting difference (ΔT_B) represents the additional temperature rise caused by the applied charge current profile:

$$\Delta T_B = T_{BR(T)} - T_{BR(P)}. \tag{12}$$

Fig. 16(a) shows the additional temperature rise for NCR when charge current ripples are superimposed on an average charge current of 813 mA. ΔT_B increases with higher ripple amplitudes due to the additional energy lost across the internal resistance by the ac ripples. Ripple frequency, on the other hand, has minimal impact on ΔT_B. Among the ripple waveforms tested, pulse ripples have the highest temperature rise because they result in the most energy loss. These temperature results for NCR align with the previous findings presented in Fig. 13 as lower improved energy efficiency corresponds to higher heat dissipation.

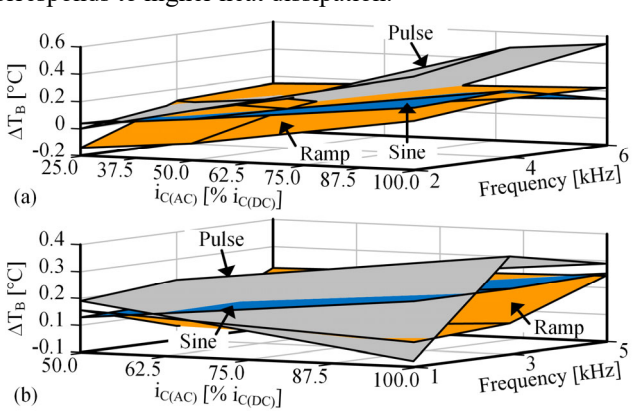

Fig. 16. Effect of ripples on battery temperature. (a) NCR. (b) IMR.

Fig. 16(b) shows that applying charge current ripples with an average charge current of 1 A for IMR does not result in a significant reduction in battery temperature rise. The trends are indistinguishable in this case because IMR has a small internal resistance, which leads to minimal ohmic loss and heating. No significant reduction in battery temperature rise is observed. Therefore, ripple charge current is ineffective in reducing battery heating during the charging process.

C. Other Considerations

Charge-Carrier Loss: Loss of charge carriers can contribute to energy loss and degrade $\%\eta_E$, which affects the accuracy of the energy efficiency results. To characterize the effect of charge-carrier loss, charge efficiency η_q is calculated using

$$\eta_q \equiv \frac{q_D}{q_C} = \frac{\int_0^{t_D} i_D dt}{\int_0^{t_C} i_C dt}, \tag{14}$$

where q_D represents the amount of charge extracted during discharge, and q_C represents the amount of charge delivered during the charging process.

Fig. 17 presents the measured η_q for both batteries. As anticipated, all values are close to 100%. This is because the loss of charge carriers within a single cycle is negligible for both batteries since they can operate for extended cycles. Consequently, the energy loss observed in the previous sections can be attributed solely to the ohmic loss across the internal resistance rather than the loss of charge carriers.

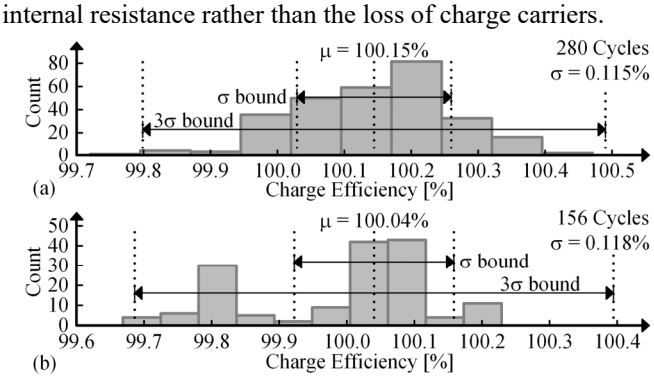

Fig. 17. Charge efficiency distribution for (a) NCR and (b) IMR.

Room temperature: Because R_B is sensitive to temperature, the results can be affected by the room temperature variations. The experiments are performed in an indoor lab with air-conditioning, so the room temperature change is small. Any significant room temperature change is expected to reflect on the battery's average temperature ($T_{B(AVG)}$) across a cycle.

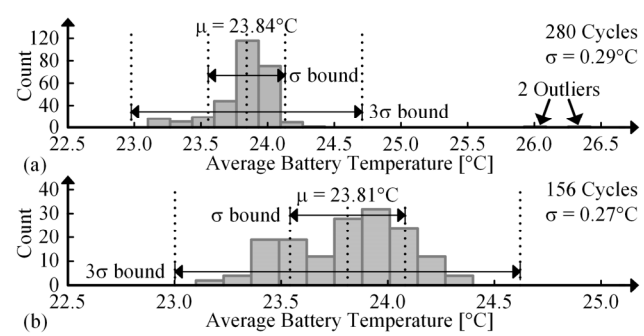

Fig. 18. Average temperature distribution for (a) NCR and (b) IMR.

Fig. 18 shows $T_{B(AVG)}$'s distribution for both batteries. The

TABLE IV
SOA LI-ION RIPPLE-CHARGING EXPERIMENTS

	[4]	[5]	[6]	[7]	[8]	This Work
Chemistry	N/A	$LiFeMgPO_4$	$LiNi_{1/3}Mn_{1/3}Co_{1/3}O_2$		N/A	$LiNi_aCo_bAl_cO_2$, $LiMn_2O_4$*
Capacity	1.5 Ah	40 Ah	25 Ah	25 Ah	3.1 Ah	3.3 Ah, 2.5 Ah
Waveform	Sine, Pulse	Sine	Sine, Ramp, Pulse	Sine	Sine, Pulse	Sine, Ramp, Pulse
Frequency [Hz]	1, 100, 10k, $f_{R(MIN)}$	1, 10, 50, 100, 300, 400, 500, 600, $f_{R(MIN)}$	$f_{R(MIN)}$	60, 100, 125, 200	N/A	1k, 2k, 3k, 4k, 5k, 6k, 7k, 8k, 9k, 10k
AC Amplitude [% $i_{C(DC)}$]	100	10, 50, 75, 100	60	50, 100	100	10, 25, 50, 100
DC Amplitude	1C	0.375C, 0.25C	1C	1C	0.5C	0.25C, 0.1875C, 0.125C 0.4C*, 0.2C*
Charge Region	No	No	No	No	No	Precondition/Test
Cycle Life	No	No	No	No	No	Yes
Energy Efficiency	N/A	N/A	No Significant Difference	No Significant Difference	N/A	CC–CV > Ramp > Sine > Pulse
Charge Time	Sine < Pulse < CC–CV	Sine < CC–CV	No Difference	No Difference	No Difference	No Difference
Temperature	Sine < Pulse < CC–CV	N/A	CC–CV ≈ Sine ≈ Ramp < Pulse	CC–CV < Sine	CC–CV < Sine < Pulse	CC–CV < Ramp ≈ Sine < Pulse

*Parameters for IMR only.

majority of $T_{B(AVG)}$ values fall within 23 °C to 24.5 °C, with only two outliers. $T_{B(AVG)}$'s mean is approximately 23.8 °C, and the standard deviation is less than 0.3 °C for both batteries. Therefore, the temperature's impact on measurement results across different cycles is small and consistent.

D. Comparison with the SoA

Table IV compares SoA experiments that investigate Li-ion battery's optimal charge current profiles. [4] was the first to propose sinusoidal-ripple-current charging based on Li-ion battery's ac resistance spectrum. It explored the impact of ripple frequency and waveform, revealing that charging with a current ripple improves both charge time and heating. [5] conducted a detailed investigation on sinusoidal ripples, varying both the ripple amplitude and frequency. The results demonstrated reduced charge time when sinusoidal ripples were applied, which corroborates the findings of [4].

However, the improvements observed in [4] and [5] were not replicated in the study conducted in [6]–[8], nor in this current study. [6] examined various charge ripple waveforms at the frequency that minimizes the battery's ac resistance, with fixed ripple amplitude. The study found no significant improvement in charge time, battery heating, or energy consumption. In fact, applying pulse ripples to the charge current resulted in additional heating. Similarly, [7] explored sinusoidal charge ripples of varying frequency and amplitude. No significant difference in charge time and energy consumption is found compared to the traditional CC-CV charging, and increased heating is observed. [8] applied sine and pulse ripples with fixed amplitude to the charge current, but observed no reduction in charge time, accompanied by increased heating as well.

The previous studies are deemed incomplete because they focused on specific ripple current profiles and lacked generalizability due to different experiment setups. In contrast, this work investigates sine, ramp, and pulse ripples of various amplitudes across frequencies for two battery types, providing the most comprehensive current profile investigation. Furthermore, the previous studies did not account for the battery's cycle-life effect, which can influence result accuracy. This study normalizes the battery's cycle-life effect at each test point to ensure accurate results. Finally, the previous studies yielded conflicting outcomes regarding the effectiveness of ripple charge current. This work contributes a wealth of data points which collectively conclude that ripple-current charging is ineffective to reduce the energy loss and heating when charging the Li-ion batteries in consumer electronics.

VI. CONCLUSIONS

This work aims to enhance the charging efficiency to meet the requirements for charging consumer electronics on the go by optimizing the charge current profiles for Li-ion batteries. The charge current profile experiments presented is the most comprehensive among the SoA, with over 400 charge-discharge cycles conducted on two Li-ion batteries. The study addresses the limitations of previous research by normalizing the battery's cycle-life effect for improved result accuracy.

The findings indicate that shaping the charge current to contain an ac ripple is ineffective in reducing the energy loss during a charge cycle. On the other hand, lower average charge currents are shown to enhance charging efficiency. Based on these findings, it is recommended to use a dc charge current that is programmed to reduce when extended charge time is available to reduce the energy loss when charging consumer electronics.

ACKNOWLEDGMENT

The authors thank Dr. Y. Barsukov, Dr. A. Blanco, Dr. O. Lazaro, Dr. J. Morroni, Dr. N. Xing, and Texas Instruments for their support.

REFERENCES

[1] "Energy Density of Lithium-ion Battery Packs, 2008-2020," ed. Energy.gov. [Online]. Office of Energy Efficiency and Renewable Energy, April 2018.

[2] A. Manthiram, "An Outlook on Lithium Ion Battery Technology," *ACS Central Science,* vol. 3, no. 10, pp. 1063-1069, Oct. 2017.

[3] F. He, *USB Port and power delivery: An overview of USB port interoperabiliy*. 2015, pp. 1-5.

[4] L. R. Chen, S. L. Wu, D. T. Shieh, and T. R. Chen, "Sinusoidal-Ripple-Current Charging Strategy and Optimal Charging Frequency Study for Li-Ion Batteries," *IEEE Transactions on Industrial Electronics,* vol. 60, no. 1, pp. 88-97, 2013.

[5] Y. D. Lee and S. Y. Park, "Electrochemical State-Based Sinusoidal Ripple Current Charging Control," *IEEE Transactions on Power Electronics,* vol. 30, no. 8, pp. 4232-4243, 2015.

[6] A. Bessman *et al.*, "Challenging Sinusoidal Ripple-Current Charging of Lithium-Ion Batteries," *IEEE Transactions on Industrial Electronics,* vol. 65, no. 6, pp. 4750-4757, 2018.

[7] S. Vadivelu, "Investigation of Sinusoidal Ripple Current Charging Techniques for Li-Ion Cells," KTH Royal Intitute of Technology, 2016.

[8] S. Y. Cho, I. O. Lee, J. I. Baek, and G. W. Moon, "Battery Impedance Analysis Considering DC Component in Sinusoidal Ripple-Current Charging," *IEEE Transactions on Industrial Electronics,* vol. 63, no. 3, pp. 1561-1573, 2016.

[9] A. Barai, G. H. Chouchelamane, Y. Guo, A. McGordon, and P. Jennings, "A study on the impact of lithium-ion cell relaxation on electrochemical impedance spectroscopy," *Journal of Power Sources,* vol. 280, pp. 74-80, April 2015.

[10] Q. Zhi, G. A. Rincón-Mora, and P. Gu, "Autonomous and Programmable 12-W 10-kHz Single-Cell Li-Ion Battery Tester," *IEEE Transactions on Instrumentation and Measurement,* vol. 71, pp. 1-8, 2022.

[11] A. Manthiram, "A reflection on lithium-ion battery cathode chemistry," *Nature Communications,* vol. 11, no. 1, p. 1550, March 2020.

[12] N. Nitta, F. Wu, J. T. Lee, and G. Yushin, "Li-ion battery materials: present and future," *Materials Today,* vol. 18, no. 5, pp. 252-264, June 2015.

[13] Y. Mekonnen, A. Sundararajan, and A. I. Sarwat, "A review of cathode and anode materials for lithium-ion batteries," in *SoutheastCon*, pp. 1-6, April 2016.

[14] Q. Wang, B. Mao, S. I. Stoliarov, and J. Sun, "A review of lithium ion battery failure mechanisms and fire prevention strategies," *Progress in Energy and Combustion Science,* vol. 73, pp. 95-131, July 2019.

[15] Y. Chen *et al.*, "A review of lithium-ion battery safety concerns: The issues, strategies, and testing standards," *Journal of Energy Chemistry,* vol. 59, pp. 83-99, Aug. 2021.

[16] S. K. Heiskanen, J. Kim, and B. L. Lucht, "Generation and Evolution of the Solid Electrolyte Interphase of Lithium-Ion Batteries," *Joule,* vol. 3, no. 10, pp. 2322-2333, Oct. 2019.

[17] D. Ouyang, M. Chen, J. Liu, R. Wei, J. Weng, and J. Wang, "Investigation of a commercial lithium-ion battery under overcharge/over-discharge failure conditions," *RSC Advances,* vol. 8, no. 58, pp. 33414-33424, 2018.

[18] D. Juarez-Robles, A. A. Vyas, C. Fear, J. A. Jeevarajan, and P. P. Mukherjee, "Overcharge and Aging Analytics of Li-Ion Cells," *Journal of The Electrochemical Society,* vol. 167, no. 9, p. 090547, June 2020.

[19] R. Guo, L. Lu, M. Ouyang, and X. Feng, "Mechanism of the entire overdischarge process and overdischarge-induced internal short circuit in lithium-ion batteries," *Scientific Reports,* vol. 6, no. 1, p. 30248, July 2016.

[20] H. Maleki and J. N. Howard, "Effects of overdischarge on performance and thermal stability of a Li-ion cell," *Journal of Power Sources,* vol. 160, no. 2, pp. 1395-1402, Oct. 2006.

[21] Y. Preger *et al.*, "Degradation of Commercial Lithium-Ion Cells as a Function of Chemistry and Cycling Conditions," *Journal of The Electrochemical Society,* vol. 167, no. 12, p. 120532, Sep. 2020.

[22] S. Ma *et al.*, "Temperature effect and thermal impact in lithium-ion batteries: A review," *Progress in Natural Science: Materials International,* vol. 28, no. 6, pp. 653-666, Dec. 2018.

[23] W. Chang, C. Bommier, T. Fair, J. Yeung, S. Patil, and D. Steingart, "Understanding Adverse Effects of Temperature Shifts on Li-Ion Batteries: An Operando Acoustic Study," *Journal of The Electrochemical Society,* vol. 167, no. 9, p. 090503, Feb. 2020.

[24] M. Petzl, M. Kasper, and M. A. Danzer, "Lithium plating in a commercial lithium-ion battery – A low-temperature aging study," *Journal of Power Sources,* vol. 275, pp. 799-807, Feb. 2015.

[25] F. Leng, C. M. Tan, and M. Pecht, "Effect of Temperature on the Aging rate of Li Ion Battery Operating above Room Temperature," *Scientific Reports,* vol. 5, no. 1, p. 12967, Aug. 2015.

[26] S. Saxena, Y. Xing, and M. Pecht, "Thermal Runaway Characterization of Li-Ion Batteries Under External Heating Conditions," *ECS Meeting Abstracts,* vol. MA2017-02, no. 4, p. 383, Sep. 2017.

[27] N. E. Galushkin, N. N. Yazvinskaya, and D. N. Galushkin, "Mechanism of Thermal Runaway in Lithium-Ion Cells," *Journal of The Electrochemical Society,* vol. 165, no. 7, p. A1303, May 2018.

[28] I. B. Espedal, A. Jinasena, O. S. Burheim, and J. J. Lamb, "Current Trends for State-of-Charge (SoC) Estimation in Lithium-Ion Battery Electric Vehicles," *Energies*, vol. 14, no. 11.

[29] R. Xiong, Y. Pan, W. Shen, H. Li, and F. Sun, "Lithium-ion battery aging mechanisms and diagnosis method for automotive applications: Recent advances and perspectives," *Renewable and Sustainable Energy Reviews,* vol. 131, p. 110048, Oct. 2020.

[30] C. Lin, A. Tang, H. Mu, W. Wang, and C. Wang, "Aging Mechanisms of Electrode Materials in Lithium-Ion Batteries for Electric Vehicles," *Journal of Chemistry,* vol. 2015, p. 104673, June 2015.

[31] M. Messing, T. Shoa, and S. Habibi, "Lithium-Ion Battery Relaxation Effects," in *IEEE Transportation Electrification Conference and Expo (ITEC)*, pp. 1-6, June 2019.

[32] X. Huang *et al.*, "A Review of Pulsed Current Technique for Lithium-ion Batteries," *Energies*, vol. 13, no. 10.

[33] A. Barai, K. Uddin, W. D. Widanage, A. McGordon, and P. Jennings, "A study of the influence of measurement timescale on internal resistance characterisation methodologies for lithium-ion cells," *Scientific Reports,* vol. 8, no. 1, p. 21, Jan. 2018.

[34] G. A. Rincon-Mora, *Analog IC Design: An Intuitive Approach*. 2019.

Qian Zhi received his B.S. degree from Georgia Tech and is currently pursuing an M.S. degree in Electrical and Computer Engineering with the Georgia Tech Analog, Power, and Energy IC research team (GTAPE). His research interests include switch-mode power supplies, battery management systems, and analog IC design.

Gabriel A. Rincón-Mora (StM'90, GSM'93, M'97, SM'01, F'11) is Motorola Solutions Foundation Professor at the Georgia Institute of Technology, Fellow of the National Academy of Inventors, and Fellow of the Institution of Engineering and Technology. He's been at Georgia Tech since 2001 and with Texas Instruments in 1994–2003. Some distinctions include the National Hispanic in Technology Award, Charles E. Perry Visionary Award, Three-Year Patent Award, Orgullo Hispano Award, and Hispanic Heritage Award. His body of work includes 11 books, 8 handbooks, 4 book chapters, 43 patents, over 190 articles, 25 videos, over 26 commercial products, and over 160 keynotes, speeches, and seminars.